**Supplementary Information for**

# The underappreciated role of anthropogenic sources in atmospheric soluble iron flux to the Southern Ocean

Mingxu Liu[1,*], Hitoshi Matsui[1,*], Douglas S. Hamilton[2], Kara D. Lamb[3,4], Sagar D. Rathod[5], Joshua P. Schwarz[4], Natalie M. Mahowald[2]

[1]Graduate School of Environmental Studies, Nagoya University, Nagoya, Japan.

[2]Department of Earth and Atmospheric Science, Cornell University, Ithaca, NY, USA.

[3]Cooperative Institute for Research in the Environmental Sciences, University of Colorado, Boulder, CO, USA.

[4]Chemical Sciences Division, NOAA Earth System Research Laboratory, Boulder, CO, USA.

[5]Department of Atmospheric Science, Colorado State University, Fort Collins, CO, USA.

***Corresponding author:** liu.mingxu@a.mbox.nagoya-u.ac.jp (M.L.) and matsui@nagoya-u.jp (H.M.)

**This PDF file includes:**

## Supplementary Note 1

### Comparison of soluble iron deposition with previous studies

Here, we put our results in the context with previous studies (Supplementary Table 1). On a global scale, we simulated a dominant role of dust in soluble iron deposition, in line with many previous studies, except Wang *et al.*[1]. Our simulated soluble iron deposition from combustion sources (0.076 Tg $yr^{-1}$) is within the range of other estimates (0.048–0.14 Tg $yr^{-1}$); that from dust sources is similar with most of previous estimates. Regarding the Southern Ocean, the soluble iron deposition from dust estimated in our study is lower than several estimates, probably because the new iron processing module that produced the solubility data used here adopted a lower initial solubility of mineral dust iron at emission than other iron modules[2]. The fact that previous iron models have overrepresented iron solubility close to dust sources points to low solubility of dust iron at emission[3]. The estimates for combustion sources (5.7 Gg $yr^{-1}$) is within the range of reported values (5.4–16 Gg $yr^{-1}$).

Importantly, this study underscores a primary contribution of anthropogenic sources to total soluble iron deposition to the Southern Ocean. We estimate the percentage contribution of anthropogenic iron about 60% to the total based on updated anthropogenic combustion emissions. However, in the simulation using anthropogenic iron inventory developed by Luo *et al.*[4], in which anthropogenic iron emissions in the Southern Hemisphere were about one-fifth those in the CTRL simulation, the anthropogenic contribution was only 11%. The relative importance of anthropogenic, dust, and biomass burning sources depends on the emissions and on the treatment of their iron solubilities. For example, Wang *et al.*[1] have suggested the contribution of combustion sources is dominant in global ocean basins because they assume a low constant fractional solubility (0.44%) of dust iron but much higher solubility of iron from fossil fuels and biomass burning (18–79%). Rathod *et al.*[5], who used the same anthropogenic

iron inventory as in our study but doubled global iron emissions from BB, found the anthropogenic contribution to soluble iron deposition to the Southern Ocean to be under 5%. Hamilton *et al*.[6] estimated an anthropogenic contribution to the Southern Ocean (~25%) similar to our estimate (38%) in the CTRL simulation because they used similar iron emissions and solubility data with our estimate.

Considering current large uncertainties in iron solubility and its potentially impacts on the estimates of soluble iron deposition, we also employed another fractional iron solubility dataset developed by Scanza *et al*.[7]. Given the higher fractional solubility for both dust and combustion sources in this dataset, the estimated soluble iron deposition fluxes are higher in both global oceans and the Southern Ocean than those in the CTRL simulation (Supplementary Table 1). In particularly, the dust soluble iron deposition is increased by three times, resulting in the contribution from dust iron comparable to those from anthropogenic and BB iron. Nevertheless, we find that the percentage contributions of anthropogenic sources are similar for the CTRL simulation (38% vs. 40%), though the contribution of dust iron varies notably.

## Supplementary Note 2

### Summary of uncertainties in this study

We summarize here the major sources of uncertainties in the global simulation of iron-bearing aerosols and how those uncertainties might affect our results. More field observations and laboratory experiments are needed to reduce these uncertainties.

2.1 Anthropogenic iron emissions

We used a new, mineralogy-based anthropogenic iron emission inventory developed by Rathod *et al*.[5] to simulate atmospheric iron concentrations and deposition. The four major iron-bearing minerals considered in our study (magnetite, hematite, illite, and kaolinite) accounted for more

than 95% of global total anthropogenic iron emissions in this inventory. The neglect of the highly soluble ferrous and ferric sulfates, which have a negligible contribution on the global total anthropogenic iron emissions, may have resulted in underestimation of atmospheric soluble iron deposition to the open oceans because one major emission source of sulfates is shipping[5]. The current estimates of combustion iron emission fluxes remain highly uncertain primarily because the fractional iron contents of aerosol emissions for diverse fuels and technologies are not well known.

The particle size distribution of iron emissions is important for modelling iron in the atmosphere, but reported distributions differed greatly. Because magnetite dominated the total iron emissions, we used the size distribution of magnetite mass measured near continental sources in East Asia by a single-particles soot photometer (SP2) and allocated all anthropogenic iron emissions into resolved size bins[8] on a global scale. Given the size range availability of the SP2, in our simulations all iron particles emitted by anthropogenic combustion were less than 3 μm in diameter, and in the total anthropogenic iron emissions, the fraction of iron emitted as particles smaller than 1.25 μm was about 0.5. Similarly, Rathod *et al.*[5] have shown that fine (smaller than 1 μm) and coarse (1–10 μm) modes contributed almost equally to the global emissions, while they have not considered particles larger than 10 μm. The global total fine-mode anthropogenic iron emission used in our simulations (about 1.0 Tg $yr^{-1}$) was much larger than those used by previous modelling studies[1,4,9,10] (lower than 0.1 Tg $yr^{-1}$), whereas the coarse-mode emissions were similar between our simulations and previous ones (0.5–2.0 Tg $yr^{-1}$). The relative fractions of fine and coarse modes of anthropogenic iron emissions depend on applications of end-of-pipe control methods to control primary particles in the industrial and power sectors, which can vary among regions and over times[11]. Hamilton *et al.*[12] have reported that the iron emission size distribution of anthropogenic sources have shifted globally towards finer modes during the past few decades as a result of more effective abatement of coarse

particles. Because size information about iron particles is closely linked to their dry and wet removal rates in the atmospheric and hence the long-range transport to remote oceans, more measurements of iron particle size distributions near emission sources are required.

2.2 Dust and Biomass burning emissions

The ranges of current estimates of global dust and biomass burning (BB) iron emissions are still broad. For dust emissions, we used an iron content of 3.5% by mass in dust particles as prescribed in many previous studies. The global total emissions of dust and dust-related iron were 2,411 and 84 Tg $yr^{-1}$ in our simulations; both these values were generally within the ranges of previous estimates, such as the AeroCom Phase I for dust emissions[13] (500–4,400 Tg $yr^{-1}$) and the GESAMP[3] intercomparison study for iron emissions from mineral dust (38–134 Tg Fe $yr^{-1}$). We additionally note that our modelled global dust aerosol optical depth at 550 nm (0.024) is close to an observationally constrained estimate ($0.030 \pm 0.005$)[14], indicating the reasonable simulation of atmospheric dust burdens. The global iron emissions from BB sources were 1.07 Tg $yr^{-1}$, which is close to values of previous studies[3,4,6,9]. Another estimate of BB iron emissions obtained by using an improved iron processing module [2] was two times as large as that in our study. Because Dust and BB sources are important contributors to soluble iron deposition to the Southern Ocean (>30 ° S), improving our knowledge of the mass and size distributions of their emissions will benefit understanding of the role of iron in the Earth system.

In addition, for estimating the future (2010–2100) changes of soluble iron deposition to the Southern Ocean, we assumed the iron emissions from Dust and BB sources remained unchanged. However, these emissions may change in the future as a result of changes in human activities and climate. For example, the predicted increase in global surface temperature by the end of the current century might result in more frequent and intense dust events. Kok *et al.*[15]

have estimated that global dust loadings will change by –5% to 10% per degree change in global surface temperature. Future changes in BB emissions also have different signs and magnitude among previous studies. For example, the Tier 1 Shared Socioeconomic Pathway projections show that the projected global BC emissions from open fires (as a proxy for BB iron) will decrease by 0.5–35% between 2015 and 2100, driven mainly by changes in land use[16]. In contrast, it has been suggested that fire emissions will increase by 2100 as a result of a warmer climate[17,18].

2.3 Fractional solubility of iron.

The fractional solubility of iron deposited to the open oceans remains a major source of uncertainties in the quantification of soluble iron deposition fluxes. It is known that atmospheric acidic and organic ligand processing can convert insoluble iron to a soluble form during atmospheric transport. Some of these processes have been considered in previous models with varying levels of complexity, but they still cannot reproduce the high iron solubilities (~10%) observed by field campaigns over the Southern Ocean, probably because some combustion sources and their dissolution processes are not taken into account by those models[19,20]. For example, Shi *et al*.[21] have recently suggested that fog processing can efficiently convert aerosol iron from insoluble to soluble form, and should be considered in atmospheric models to capture the wide range of observed iron solubility.

In this work, we calculated soluble iron deposition offline by integrating the model iron deposition fluxes in each simulation and the fractional iron solubility at deposition provided by a global aerosol model from Hamilton *et al*.[2,12], who used the same anthropogenic iron emission inventory with our CTRL simulation. The annual mean fractional solubilities of iron deposited to the Southern Ocean were 7.3% for anthropogenic iron, 16% for BB, and 1.5% for dust. However, the use of this solubility data to estimate soluble iron deposition in the Southern

Ocean in the CTRL_HIGH simulation may introduce some uncertainties. In the CTRL_HIGH simulation, we scaled upward the anthropogenic iron emissions in the Southern Africa continent and assumed that the increases in emission did not change the iron solubility on a global scale. In fact, the soluble iron over oceans originates from iron emissions in both continental (e.g., industries) and ocean (e.g., shipping) sources[5], and the changes of continental emissions would alter the solubility of iron over remote oceans. Considering there are still large uncertainties in iron solubility for different combustion sources, we used the same solubility data for all our simulations. Note that the uncertainties in the iron solubility data used in this study were due mainly to uncertainties in the solubility at emission and in iron dissolution schemes. For example, as shown in Table 3 of Rathod *et al*.[5], the measured solubility of iron in coal fly ash reported in different studies ranged from 3% to 21%, and iron solubility in oil fly ash ranged from 8% to 85%. The reaction rates of the dissolution processes also differed greatly among iron aerosol species and fuel sources and need to be better constrained with laboratory and field experiments[2,7,22].

### 2.4 Comparison with aircraft measurements of magnetite

In this study, we evaluated the simulations of anthropogenic iron budget over the Southern Ocean by using the aircraft measurements of magnetite concentration profiles over Pacific and Atlantic Oceans. The modeled magnetite concentrations were underestimated by up to one order of magnitude in the upper troposphere (pressure level <300 hPa) over the Southern Ocean (Fig. 1). Multiple sensitivity simulations showed that an increase of anthropogenic magnetite emissions in Southern Hemisphere could effectively reduce this underestimation (Supplementary Fig. 3). Other factors, such as wet deposition efficiency and atmospheric transport, might contribute to these biases. Note that the iron dissolution of aggregated magnetite nanoparticles probably influenced measured magnetite concentrations, which was not considered in our model. The atmospheric chemical processing of iron-bearing minerals

can release dissolved iron into solutions and potentially lower the mass of aggregated minerals[23]. Considering this effect, those simulated iron oxide concentrations may further be biased low relative to the measurements, suggesting the underestimation of magnetite concentrations in the CTRL simulation attributable to the emissions errors rather than its atmospheric processing. Moreover, uncertainties in aerosol size distributions and mixing states may be important. Finer size distributions of magnetite correspond to smaller deposition fluxes near source regions and hence to enhanced long-range transport to remote areas. The treatment of multiple particle mixing states with the considerations of both fresh and aged magnetite would also increase the lifetime of magnetite particles compared to that with the single internal mixing state used in this study[24,25]. We have also discussed the uncertainties in the comparison with surface measurements of total iron concentrations in a previous study[26].

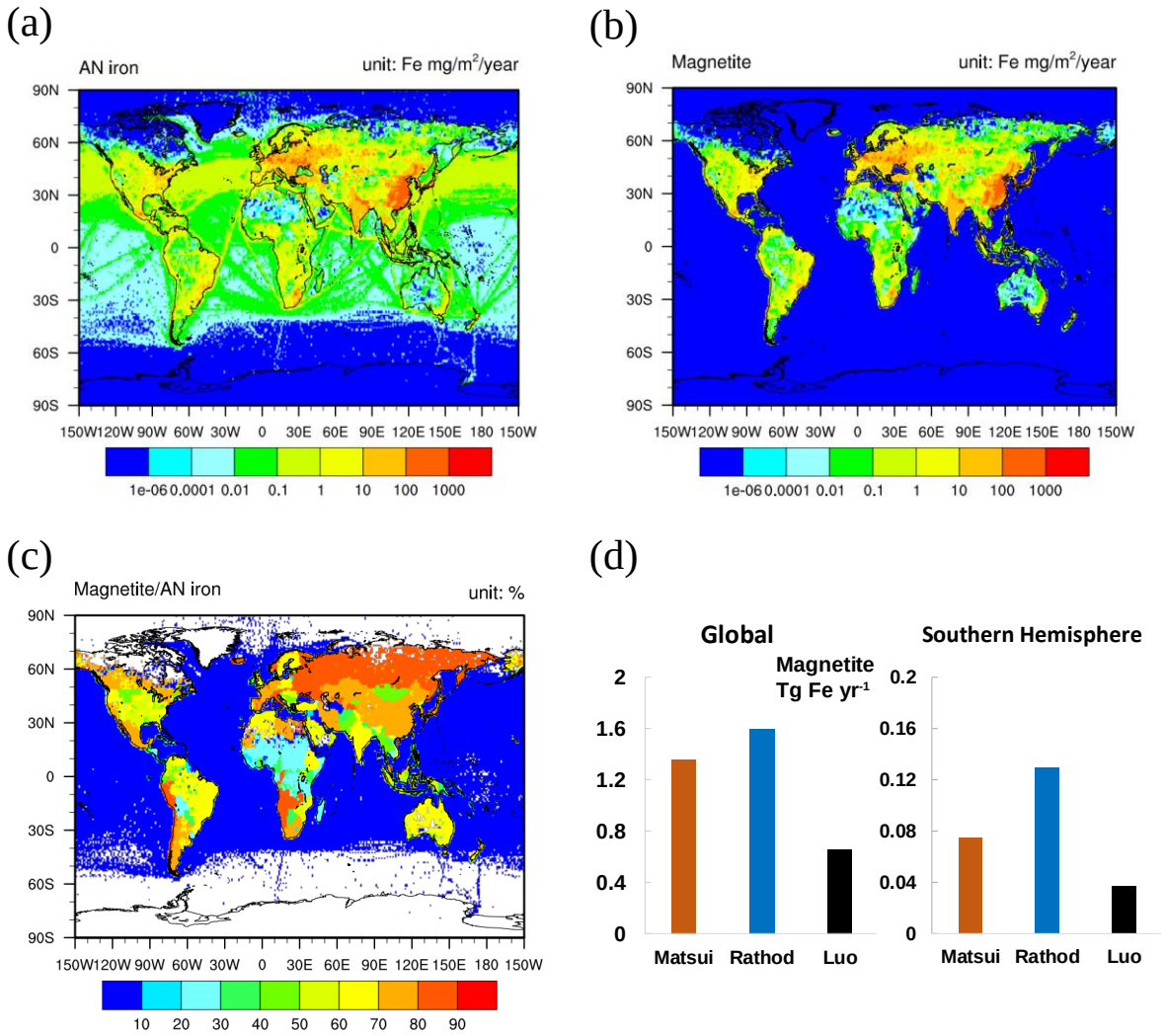


**Supplementary Fig. 1**. The AN iron emission inventory developed by Rathod et al. and comparisons with other estimates. (a, b) Maps of AN iron and magnetite emissions. Magnetite is a primary AN iron oxide and accounts for about 70% of total iron emissions globally. (c) The proportion of magnetite relative to total AN iron varies among regions and is mostly within 50–90%; (d) Comparison of estimates of AN iron emissions as magnetite. The estimates by both Matsui *et al.* [26] and Luo *et al.* [4] are lower than that by Rathod *et al.* [5], both globally and in the Southern Hemisphere. Here, we assumed that all AN iron in the Luo2008 inventory was magnetite because this inventory did not provide speciation information for AN iron.

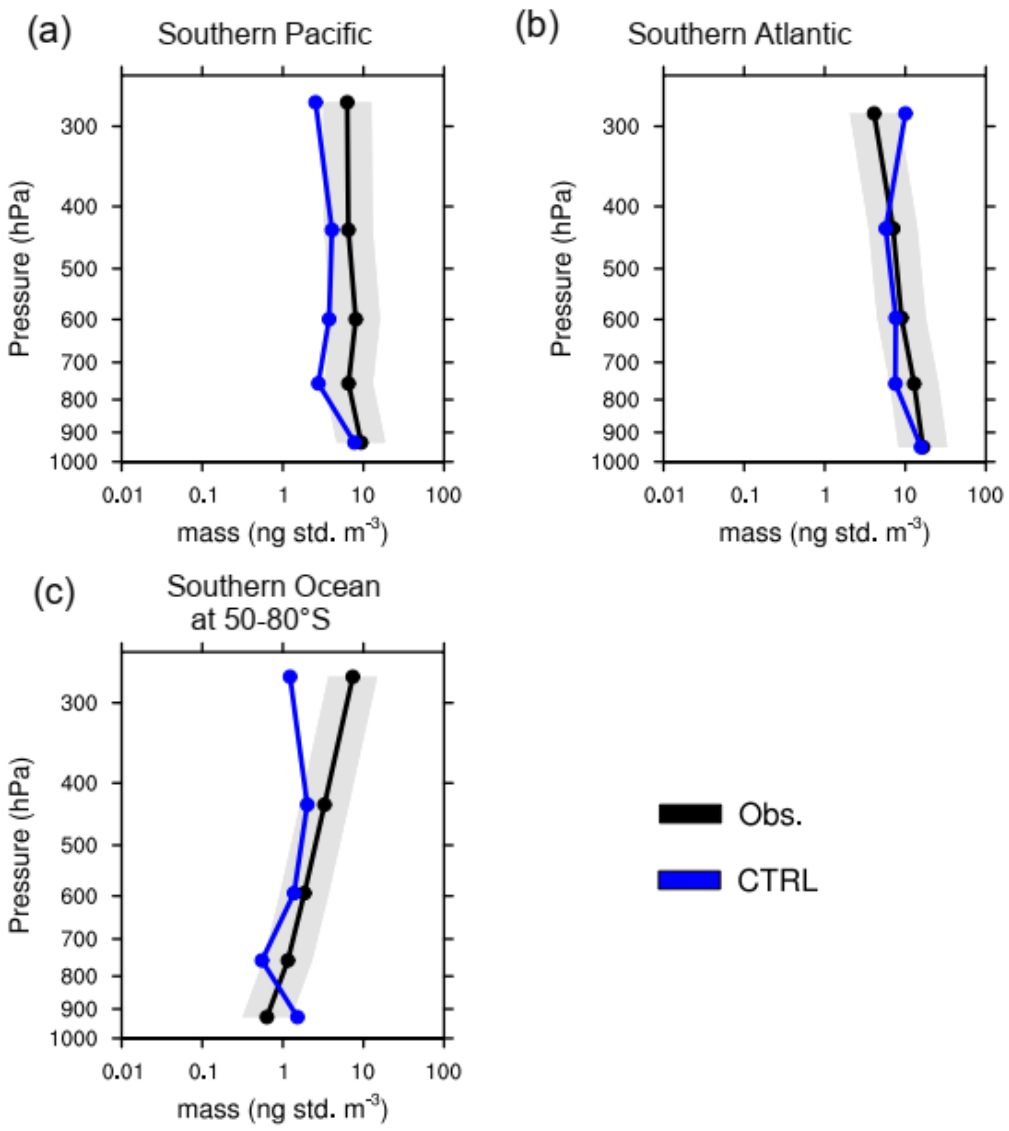


**Supplementary Fig. 2.** Comparison of simulated black carbon concentration profiles over the Southern Ocean with aircraft measurements**.** The simulation results are derived from the CTRL case. The comparisons are made over the three oceanic regions: (a) Southern Pacific (20–50° S, 160° E–135° W), (b) Southern Atlantic (20–50° S, 20–60° W), and (c) high-latitude Southern Ocean basin (50–80° S, 140° E–20° W). The grey shaded areas represent the gaps within a factor of two relative to the observation mean.

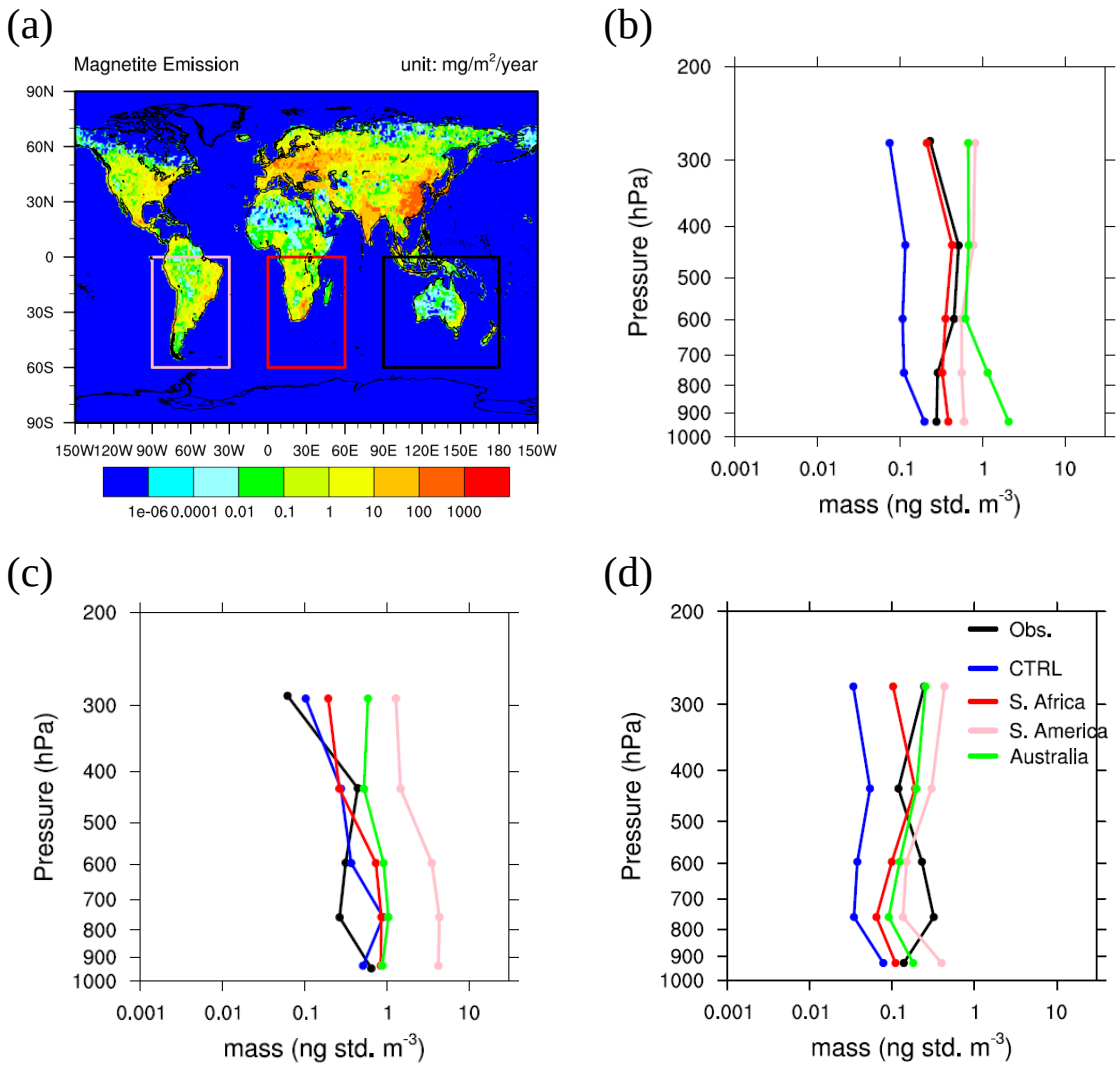


**Supplementary Fig. 3.** Comparison of anthropogenic magnetite concentration profiles over the Southern Oceans among different sensitivity simulation experiments. In addition to the CTRL simulation using the emission inventory from Rathod et al.[5], we perform three other sensitivity simulations by increasing magnetite emission fluxes by a factor of 5 separately over South America (S. America), Southern Africa (S. Africa), and Australia and the surrounding countries (pink, red, and black rectangles, respectively, from left to right in Supplementary Fig. 3a), and then compare the resulting profiles with the observations and the CTRL simulation results over Southern Pacific (b), Southern Atlantic (c), and the high-latitude Southern Ocean (d). These simulations indicate that the case with increases of the emissions in Southern Africa (red lines) shows the best agreement with observations.

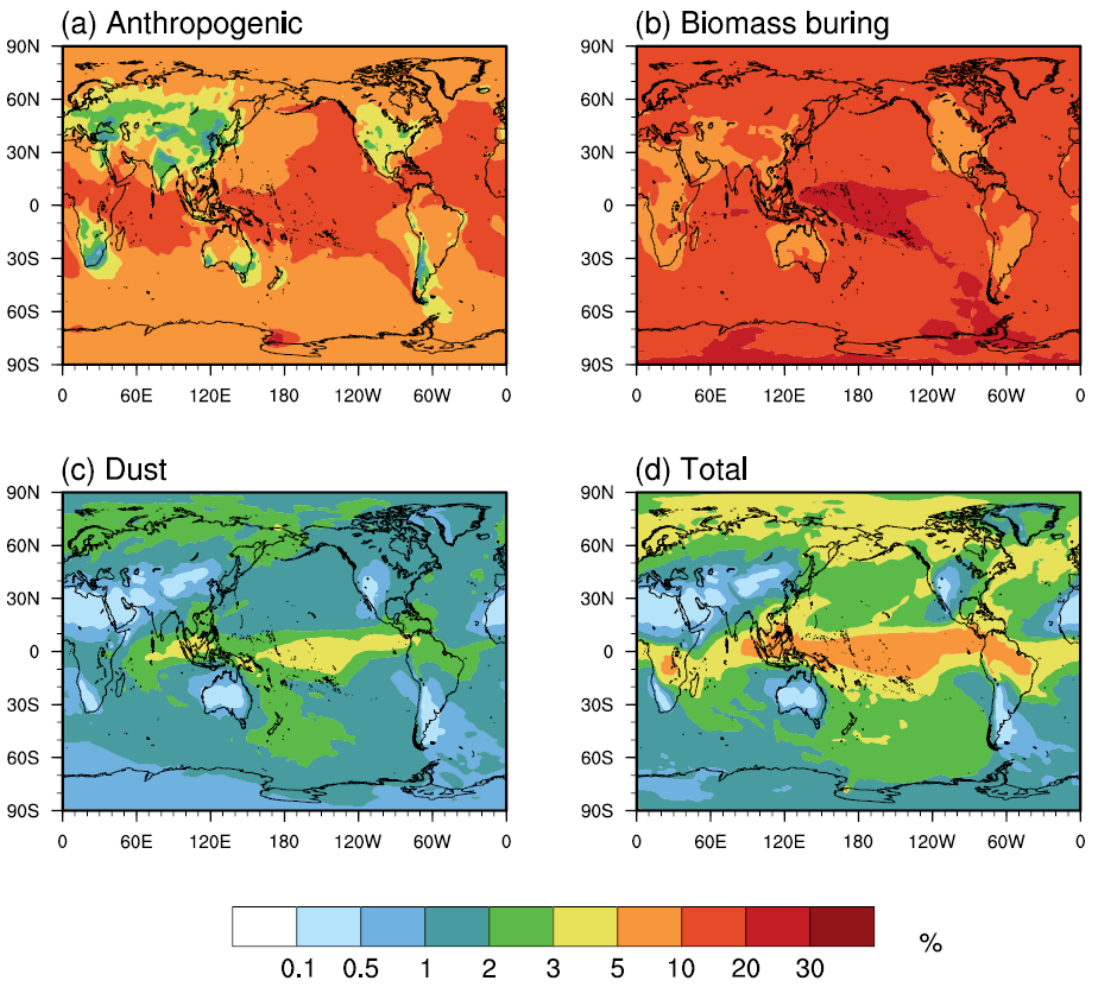


**Supplementary Fig. 4.** The global map of source-specific iron solubility (%) at deposition. The solubility data are shown separately for: (a) anthropogenic iron, (b) biomass burning iron, (c) dust iron, and (d) the total iron. The distribution of the total iron solubility resembles the solubility of dust sources because dust dominates the iron deposition to the ocean.

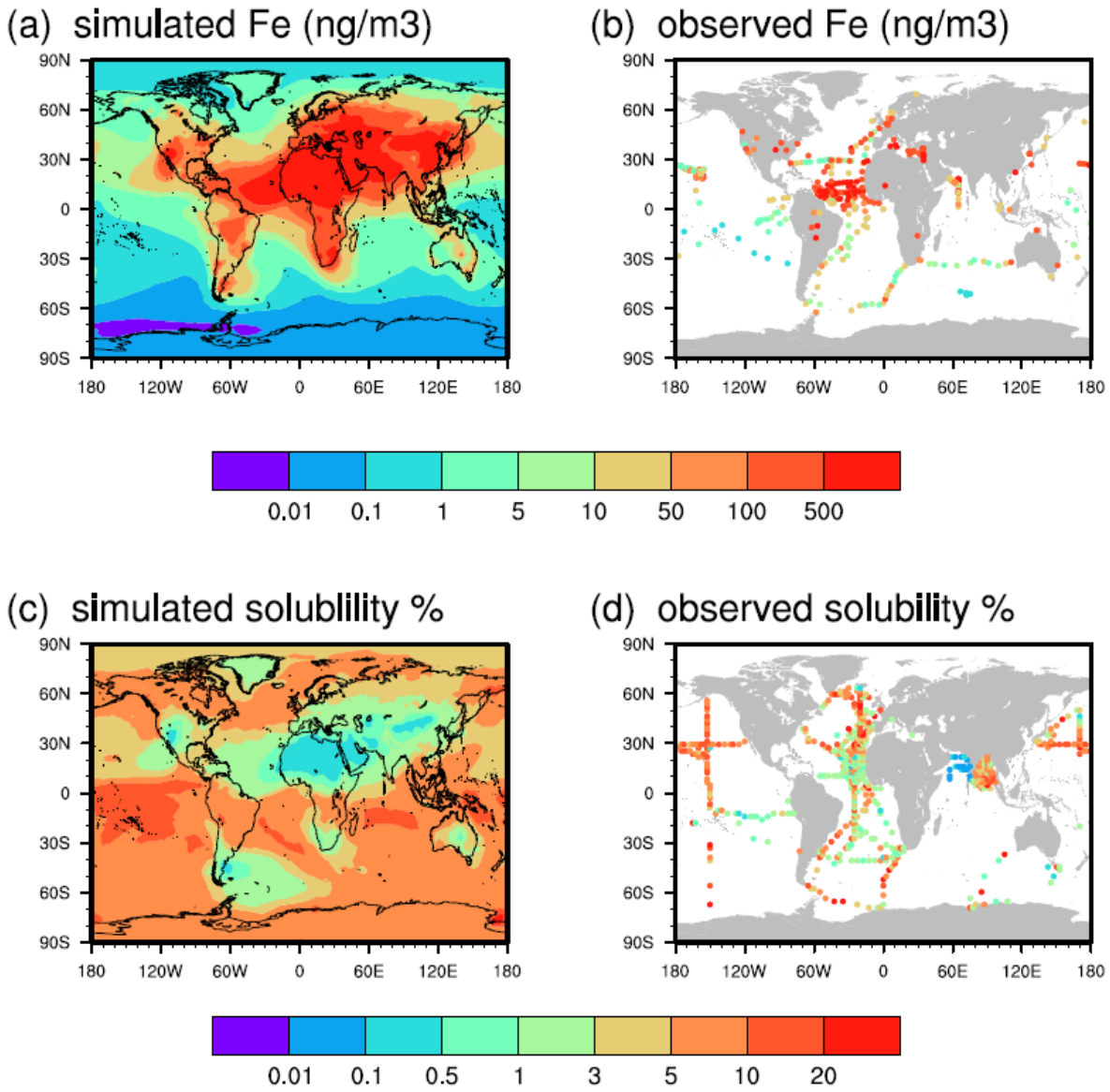


**Supplementary Fig. 5.** Comparison of near-surface total iron concentrations and the iron solubility between the CTRL_HIGH simulation and observations (unit: ng $m^{-3}$). (a-b) Comparison of simulated and observed (colored dots over the map) near-surface iron concentrations. (c-d) Comparison of simulated and observed iron solubility. The in-situ observations of total iron and solubility were provided by Mahowald *et al.*[27] and Ito *et al.*[19], respectively. Note that the iron observations shown here represented only a few days in a year, while the simulation results were based on annual averages.

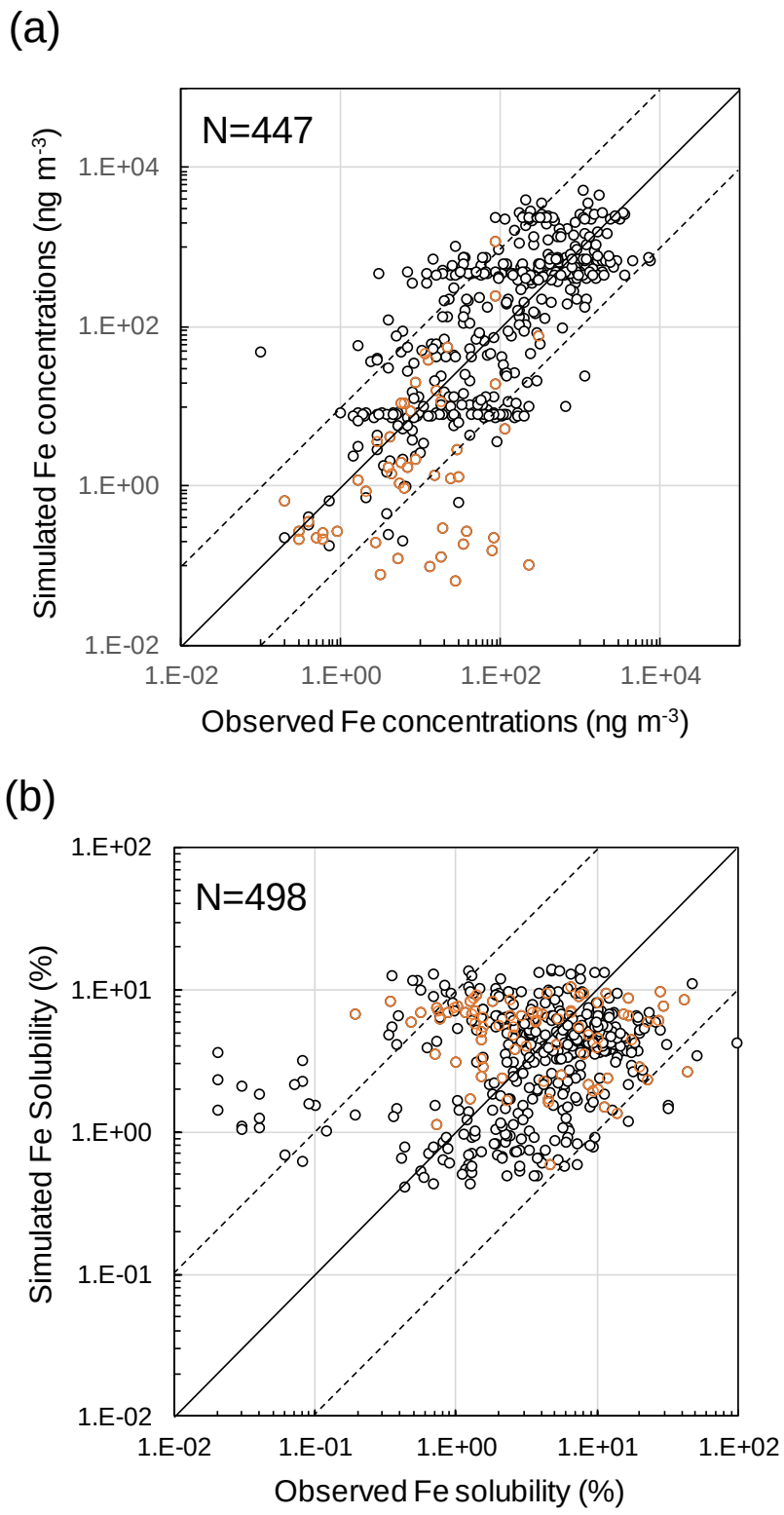


**Supplementary Fig. 6.** Scatter plots of the comparison of simulated total iron concentrations and iron solubility with the corresponding observations. (a) Comparison of iron concentrations between observations and simulations. (b) Comparison of iron solubility. The available observation stations are displayed in Supplementary Fig. 5. The solid line denotes a 1:1 correspondence and the two dashed lines denote the deviations by a factor of ±10. The data pairs for the Southern Ocean are marked in orange.

(a) CTRL

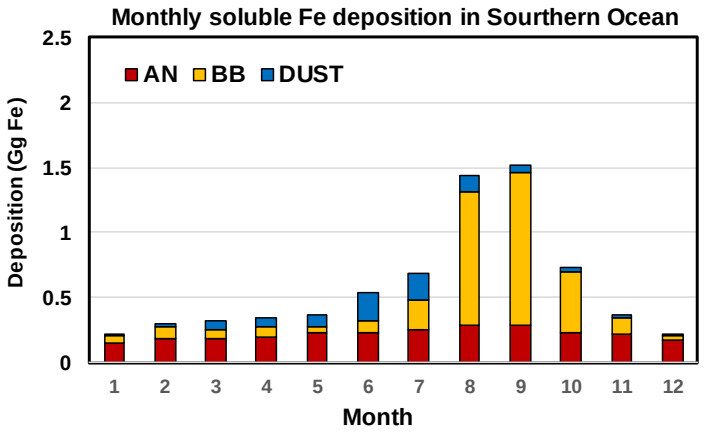


(b) CTRL_HIGH

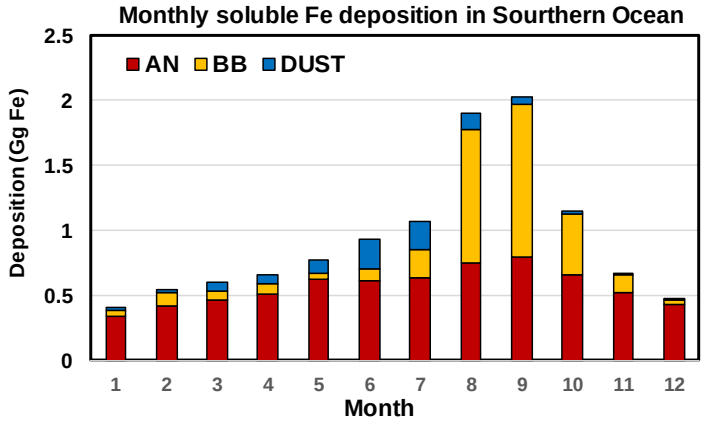


(c) Luo2008

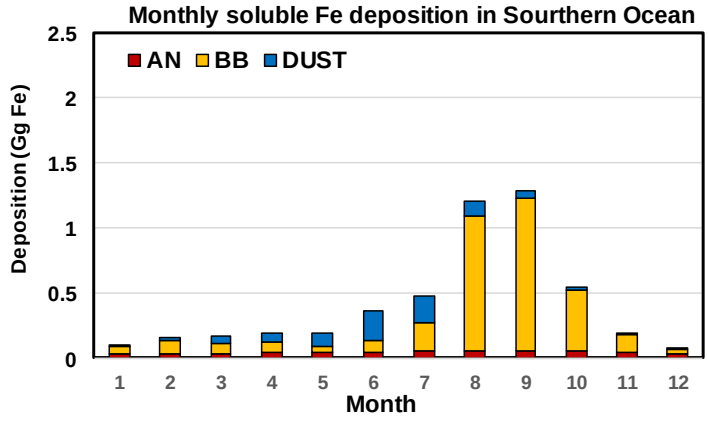


**Supplementary Fig. 7.** Monthly accumulated soluble iron deposition (unit: Gg per month) in the Southern Ocean. The simulation results are derived separately from: (a) CTRL, (b) CTRL_HIGH, and (c) Luo2008 cases. The contributions of AN sources are distinct among these cases because of the differences of the AN emission inventories used. Monthly soluble iron deposition fluxes from BB and DUST sources are the same in all simulations.

**Supplementary Table 1.** Comparison of soluble iron deposition to the global ocean and the Southern Ocean (30-90 °S) between this study and previous studies. Soluble iron deposition from combustion is the sum of from anthropogenic (AN) and biomass burning (BB) depositions.

| Region | Study | Total | Dust | Combustion | AN | BB |
|---|---|---|---|---|---|---|
| Global Oceans (Tg $yr^{-1}$) | Scanza *et al.*[7] | 0.59 | 0.54 | 0.048 | | |
| | Luo *et al.*[4] | 0.49 | 0.41 | 0.080 | | |
| | Luo and Gao[28] | 0.36 | | | | |
| | Myriokefalitakis *et al.*[3] | 0.25 | | | | |
| | Myriokefalitakis *et al.*[29] | 0.19 | | | | |
| | Rathod *et al.*[5] | | | | 0.035-0.46[a] | |
| | Hamilton *et al.*[2] | 0.53 | 0.41 | 0.12 | | |
| | Wang *et al.*[1] | 0.17 | 0.034 | 0.14 | 0.11 | 0.030 |
| | Ito et al.[30] | 0.27 | 0.224 | 0.048 | 0.015 | 0.033 |
| | Johnson and Meskhidze[31] | 0.26 | | | | |
| | Okin *et al.*[32] | 0.36 | | | | |
| | CTRL[b] | 0.27[c], 0.68[d] | 0.19, 0.59 | 0.076, 0.094 | 0.047, 0.064 | 0.029, 0.030 |
| Southern Ocean (Gg $yr^{-1}$) | Scanza *et al.* [7] | 14 | 8.7 | 5.4 | | |
| | Hamilton *et al.* [2] | 37 | 21 | 16 | | |
| | Matsui *et al.* [26] | 11 | 3.0 | 8.0 | | |
| | CTRL | 6.6[c], 10.1[d] | 0.91, 3.4 | 5.7, 6.7 | 2.5, 4.0 | 3.2, 2.7 |
| | CTRL_HIGH | 10.6 | 0.91 | 9.7 | 6.5 | 3.2 |
| | Luo2008 | 4.6 | 0.91 | 3.7 | 0.53 | 3.2 |

[a]The AN soluble iron deposition range result from different solubility data.

[b]The results are based on the CTRL simulation; The results for the Southern Ocean are shown separately for the CTRL, CTRL_HIGH and Luo2008 cases. In the CTRL case, we show two sets of the calculations based on different solubility data.

[c]The soluble iron deposition is calculated based on the iron solubility data from Hamiton *et al.* [2]

[d]The soluble iron deposition is calculated based on the iron solubility data from Scanza *et al.* [7]

## Supplementary References


1 Wang, R. *et al.* Sources, transport and deposition of iron in the global atmosphere. *Atmos. Chem. Phys.* **15**, 6247-6270 (2015).

2 Hamilton, D. S. *et al.* Improved methodologies for Earth system modelling of atmospheric soluble iron and observation comparisons using the Mechanism of Intermediate complexity for Modelling Iron (MIMI v1.0). *Geosci. Model Dev.* **12**, 3835-3862 (2019).

3 Myriokefalitakis, S. *et al.* Reviews and syntheses: the GESAMP atmospheric iron deposition model intercomparison study. *Biogeosciences* **15**, 6659-6684 (2018).

4 Luo, C. *et al.* Combustion iron distribution and deposition. *Global Biogeochem. Cycles* **22**, GB1012 (2008).

5 Rathod, S. D. *et al.* A Mineralogy ‐ Based Anthropogenic Combustion ‐ Iron Emission Inventory. *J. Geophys. Res.-Atmos* **125**, e2019JD032114 (2020).

6 Hamilton, D. S. *et al.* Impact of Changes to the Atmospheric Soluble Iron Deposition Flux on Ocean Biogeochemical Cycles in the Anthropocene. *Global Biogeochem. Cycles* **34**, e2019GB006448 (2020).

7 Scanza, R. A. *et al.* Atmospheric processing of iron in mineral and combustion aerosols: development of an intermediate-complexity mechanism suitable for Earth system models. *Atmos. Chem. Phys.* **18**, 14175-14196 (2018).

8 Moteki, N. *et al.* Anthropogenic iron oxide aerosols enhance atmospheric heating. *Nat. Commun.* **8**, 15329 (2017).

9 Ito, A. Global modeling study of potentially bioavailable iron input from shipboard aerosol sources to the ocean. *Global Biogeochem. Cycles* **27**, 1-10 (2013).

10 Ito, A., Lin, G. & Penner, J. E. Radiative forcing by light-absorbing aerosols of pyrogenetic iron oxides. *Sci. Rep.* **8**, 7347 (2018).

11 Bond, T. C. *et al.* A technology-based global inventory of black and organic carbon emissions from combustion. *J. Geophys. Res.-Atmos* **109**, D14203 (2004).

12 Hamilton, D. S. *et al.* Recent (1980 to 2015) Trends and Variability in Daily ‐ to ‐ Interannual Soluble Iron Deposition from Dust, Fire, and Anthropogenic Sources. *Geophys. Res. Lett.* **47**, e2020GL089688 (2020).

13 Huneeus, N. *et al.* Global dust model intercomparison in AeroCom phase I. *Atmos. Chem. Phys.* **11**, 7781-7816 (2011).

14 Ridley, D. A., Heald, C. L., Kok, J. F. & Zhao, C. An observationally constrained estimate of global dust aerosol optical depth. *Atmos. Chem. Phys.* **16**, 15097-15117 (2016).

15 Kok, J. F., Ward, D. S., Mahowald, N. M. & Evan, A. T. Global and regional importance of the direct dust-climate feedback. *Nat. Commun.* **9**, 241 (2018).

16 Feng, L. *et al.* The generation of gridded emissions data for CMIP6. *Geosci. Model Dev.* **13**, 461-482 (2020).

17 Ward, D. S. *et al.* The changing radiative forcing of fires: global model estimates for past, present and future. *Atmos. Chem. Phys.* **12**, 10857-10886 (2012).

18 Pechony, O. & Shindell, D. T. Driving forces of global wildfires over the past millennium and the forthcoming century. *Proc. Natl. Acad. Sci. U.S.A.* **107**, 19167 (2010).

19 Ito, A. *et al.* Pyrogenic iron: The missing link to high iron solubility in aerosols. *Sci. Adv.* **5**, eaau7671 (2019).

20 Ito, A. *et al.* Evaluation of aerosol iron solubility over Australian coastal regions based on inverse modeling: implications of bushfires on bioaccessible iron concentrations in the Southern Hemisphere. *Prog. Earth Planet. Sci.* **7**, 42 (2020).

21 Shi, J. *et al.* High Production of Soluble Iron Promoted by Aerosol Acidification in Fog. *Geophys. Res. Lett.* **47** (2020).

22 Ito, A. Atmospheric Processing of Combustion Aerosols as a Source of Bioavailable Iron. *Environ. Sci. Technol. Lett.* **2**, 70-75 (2015).

23 Chen, H. *et al.* Coal fly ash as a source of iron in atmospheric dust. *Environ Sci Technol* **46**, 2112-2120 (2012).

24 Matsui, H. & Mahowald, N. Development of a global aerosol model using a two-dimensional sectional method: 2. Evaluation and sensitivity simulations. *J. Adv. Model. Earth Syst.* **9**, 1887-1920 (2017).
25 Matsui, H. Development of a global aerosol model using a two-dimensional sectional method: 1. Model design. *J. Adv. Model. Earth Syst.* **9**, 1921-1947 (2017).
26 Matsui, H. *et al.* Anthropogenic combustion iron as a complex climate forcer. *Nat. Commun.* **9**, 1593 (2018).
27 Mahowald, N. M. *et al.* Atmospheric Iron Deposition: Global Distribution, Variability, and Human Perturbations. *Annual Review of Marine Science* **1**, 245-278 (2009).
28 Luo, C. & Gao, Y. Aeolian iron mobilisation by dustacid interactions and their implications for soluble iron deposition to the ocean: a test involving potential anthropogenic organic acidic species. *Environ. Chem.* **7**, 153-161 (2010).
29 Myriokefalitakis, S. *et al.* Changes in dissolved iron deposition to the oceans driven by human activity: a 3-D global modelling study. *Biogeosciences* **12**, 3973-3992 (2015).
30 Ito, A., Ye, Y., Baldo, C. & Shi, Z. Ocean fertilization by pyrogenic aerosol iron. *npj Clim. Atmos. Sci.* **4**, 30 (2021).
31 Johnson, M. S. & Meskhidze, N. Atmospheric dissolved iron deposition to the global oceans: effects of oxalate-promoted Fe dissolution, photochemical redox cycling, and dust mineralogy. *Geosci. Model Dev.* **6**, 1137-1155 (2013).
32 Okin, G. S. *et al.* Impacts of atmospheric nutrient deposition on marine productivity: Roles of nitrogen, phosphorus, and iron. *Global Biogeochem. Cycles* **25** (2011).